RADIAL VELOCITY ECLIPSE MAPPING OF EXOPLANETS

Nikolay Nikolov and Felix Sainsbury-Martinez
Astrophysics Group, School of Physics, University of Exeter, Stocker Road, Exeter EX4 4QL, UK; nikolay@astro.ex.ac.uk

ABSTRACT

Planetary rotation rates and obliquities provide information regarding the history of planet formation, but have not yet been measured for evolved extrasolar planets. Here we investigate the theoretical and observational perspective of the Rossiter–McLaughlin effect during secondary eclipse (RMse) ingress and egress for transiting exoplanets. Near secondary eclipse, when the planet passes behind the parent star, the star sequentially obscures light from the approaching and receding parts of the rotating planetary surface. The temporal block of light emerging from the approaching (blueshifted) or receding (redshifted) parts of the planet causes a temporal distortion in the planet's spectral line profiles resulting in an anomaly in the planet's radial velocity curve. We demonstrate that the shape and the ratio of the ingress-to-egress radial velocity amplitudes depends on the planetary rotational rate, axial tilt, and impact factor (i.e., sky-projected planet spin–orbital alignment). In addition, line asymmetries originating from different layers in the atmosphere of the planet could provide information regarding zonal atmospheric winds and constraints on the hot spot shape for giant irradiated exoplanets. The effect is expected to be most-pronounced at near-infrared wavelengths, where the planet-to-star contrasts are large. We create synthetic near-infrared, high-dispersion spectroscopic data and demonstrate how the sky-projected spin axis orientation and equatorial velocity of the planet can be estimated. We conclude that the RMse effect could be a powerful method to measure exoplanet spins.

Key words: infrared: planetary systems – planetary systems – planets and satellites: atmospheres –
planets and satellites: fundamental parameters – techniques: spectroscopic

1. INTRODUCTION

Planetary rotation rates and axial tilts are critical parameters in determining seasonal climate variations (Williams & Kasting 1997; Cowan et al. 2012) and are relevant to the planet formation and evolution history (Agnor et al. 1999). By definition, the planet rotational rate and axial tilt (e.g., obliquity) are respectively the time it takes for a complete revolution and the angle between the planetary spin angular momentum and the planet's orbital angular momentum. Planets with obliquity <90° and >90° are considered to have prograde and retrograde rotation, respectively. Planet spins are well-constrained for the solar system planets, spanning a wide range of rotational rates and axial tilts (Cox & Pilachowski 2000) and are considered to reflect the unique formation and evolutionary history of each planet (Laskar & Robutel 1993). Planets accumulate rotational angular momentum from the relative motions of accreted material. The stochastic nature of planetary accretion from planetesimals allows for a random component to the net spin angular momentum. Prograde angular momentum (i.e., spin) could be accumulated by a planet on a circular orbit within a uniform surface density disk of small planetesimals. The planet clears a gap and thus accretes a larger fraction of material from the edges of its accretion zone. Retrograde spins are considered to originate from giant impacts during the early stages of planet formation. Therefore constraints on the planet spins are of high scientific interest, because deviations of the axes of rotation may have been caused by impacts of large bodies during their early history. Even the axes of rotation of the gaseous planets may have been affected by impacts on their rocky cores before these planets accumulated their large atmospheres of hydrogen and helium. Such atmospheres are considered to be accreted hydrodynamically, in flows quite different from those which govern the dynamics of

planetesimals and lead to prograde rotation (de Pater & Lissauer 2001; Faure & Mensing 2007).

Exoplanet tidal theory predicts obliquity erosion, on time scales <1 Gyr, for planets on ≲10 day orbits around normal low-mass stars, i.e., preventing seasonal variations (Heller et al. 2011a, 2011b). Observational methods have been proposed to probe the rotation rates and obliquities for exoplanets from oblateness measurements and variability due to surface inhomogeneity, e.g., Hui & Seager (2002), Seager & Hui (2002), Barnes & Fortney (2003), Pallé et al. (2008), Kawahara & Fujii (2010), and Fujii & Kawahara (2012), but require precisions in excess of ∼0.1 μmag.

Currently a rotational rate has been probed for only one extrasolar planet—the young fast rotator β Pic b, (Snellen et al. 2014) while axial tilts have not yet been measured. Ground-based high-dispersion spectroscopy ($R \geqslant 20,000$) in the near-infrared has recently become successful in characterizing the atmospheres of hot Jupiters (Snellen et al. 2010; Brogi et al. 2012, 2014; Birkby et al. 2013; Schwarz et al. 2015). At high spectral resolution molecular absorption bands are resolved into individual lines allowing their robust identification by line matching with model templates. As the planet orbits its star, the radial component of the planet orbital velocity changes by tens of km s^{-1}, enabling a discrimination of the Doppler shifted planet spectrum from the steady telluric contamination. The planet signal is then extracted by cross-correlating the data with model spectra obtained by mixing the expected spectroscopically active trace gases in hot-Jupiter atmospheres and assuming a range of vertical temperature pressure profiles.

Kawahara (2012) considered the effect of planetary spin on the planetary radial velocity in dayside spectra of exoplanets, simulated the effect and concluded that planetary radial velocity could be a powerful means for constraining planet

spins. In this paper we describe the potential of the Rossiter–McLaughlin effect during secondary eclipse (RMse) combined with near-infrared high-dispersion spectroscopy to provide constraints on exoplanet rotation and obliquity.

The rest of the paper is organized as follows. Section 2 describes the rotational effect in transiting exoplanets. In Section 3 we derive the planet radial velocity anomaly due to the RMse effect. We choose the methodology of Ohta et al. (2005) who found an analytic solution for the RM effect at primary transits and show that their solution can equivalently be applied to the problem discussed here. Section 4 details the amplitude and shape of the RMse effect and discusses potential targets. Section 5 discusses the potential application of the method in light of the available and future instrumentation. Finally Section 6 is devoted to our conclusions.

2. RM EFFECT AT PLANET SECONDARY ECLIPSE

In its nature, the RM effect arises because of stellar rotation (McLaughlin 1924; Rossiter 1924). During a stellar occultation or a planetary transit, portions of the rotating star surface are temporarily obscured, causing the removal of particular radial velocity components from the stellar broadened absorption lines leading to a temporal radial velocity anomaly (Winn et al. 2005). The same effect is expected to take place with a rotating planet at secondary eclipse. When the planet passes behind the parent star the light from the approaching and receding parts of the rotating planetary surface sequentially enter/exit the geometric shadow of the star. The temporal block of light emerging from the approaching (blueshifted) or receding (redshifted) parts of the planet causes temporal distortion in the line profiles of the planet's spectrum leading to an anomaly in the planet radial velocity curve. The shape and amplitude of this anomaly depend on the planet rotation rate, axial tilt and spatial orientation (i.e., planet spin–orbital alignment). Measurements of rotational rates and axial tilts are of high scientific interest as they provide constraints on exoplanet formation and evolution.

3. FORMALISM OF THE EFFECT

To describe quantitatively the radial velocity anomaly caused by the RMse effect we assume a two-body problem with a central star and a planet of masses m_s and m_p, respectively. We refer the reader to Figure 1 in Ohta et al. (2005) for a schematic illustration of the top view of the planetary orbit and their Equations (1)–(7). The orbital velocity of the planet as a function of time with respect to the star, up to $O(e)$ as detailed in Murray & Dermott (1999) is

$$v_{\mathrm{rad,p}} \approx \frac{m_s}{m_s + m_p} na \sin i \left[\sin(M + \varpi) + e \sin(2M + \varpi) \right], \quad (1)$$

with all quantities defined in Table 1.

An eclipse or occultation of a part of the rotating planetary surface causes a time-dependant asymmetry in the absorption/emission line profiles. These asymmetries result in an apparent shift of the central spectral line positions when the lines are unresolved.

To describe the radial velocity anomaly caused by the planet rotation, similar to Ohta et al. (2005), we initially set the coordinate system at the star center and its y-axis to coincide

Table 1
List of Notation

Variables	Definition	Meaning
		Orbital Parameters
m_s	Section 3	Star mass
m_p	Section 3	Planet mass
P	Section 3	Orbital period
a	Figure 1*	Semimajor axis
e	Figure 1*	Planet orbital eccentricity
ϖ	Figure 1*	Argument of periastron
E	Figure 1*	Eccentric anomaly
n	Figure 1*	Mean motion
M	Figure 1*	Mean anomaly
τ	Figure 1*	Time of pericenter passage
i	Figure 1(a)	Orbital inclination
f	Figure 1(a)	True anomaly
r_p	Figure 1(a)	Planet to star distance
		Internal Parameters of Star and Planet
I_p	Figure 1(a)	Planet spin-to-y-axis angle
Ω_p	Figure 1(a)	Planet angular velocity
λ_p	Figure 1(b)	Sky-projected spin–orbit angle
R_s	Section 3	Stellar radius
R_p	Section 3	Planet radius
V_p	Section 3	Planet surface velocity, $R_p\Omega_p$
		Mathematical Notation
$\hat{n}_p$	Figures 1(a), (b)	Normal vector to the planet orbit
x_s	Section 3	Position of the star
x_p	Section 3	Position of the planet
γ	Section 3	Star to planet ratio R_*/R_p
η_s	Equation (7)	See Figure 1(c)
x_0	Equation (12)	See Figure 1(c)
z_0	Equation (13)	See Figure 1(c)
ζ_s	Equation (14)	See Figure 1(c)

Note. See Figure 1 in Ohta et al. (2005) for all quantities marked with (*) and are defined as expected.

with the observer's line of sight (Figure 1(a)). The planet position is described with the coordinates (x_p, z_p), corresponding to the orbit plane position and the planet impact parameter.

For simplicity of the mathematical description of the problem, we choose a reference system (x', z') centered on the planet and rotated such that the z'-axis is parallel to the rotation axis of the planet (i.e., parallel to Ω_p, see Figure 1(b)) and the rotation axis lies in the y'–z' plane. We define an angle λ_p between the sky-projected rotational angular velocity and the normal unit vector of the planet orbit, $\hat{n}_p$, see Figure 1(b). This differs from the definition of Ohta et al. (2005), who assume λ to be the angle between the sky-projected stellar rotation axis Ω_s and the normal vector of the planetary orbit $\hat{n}_p$.

In all calculations we ignore differential rotation of the planet surface as well as motions associated with atmospheric dynamics. A point on the surface of the rotating planet with coordinates (x', z') will move with a velocity v_p given by

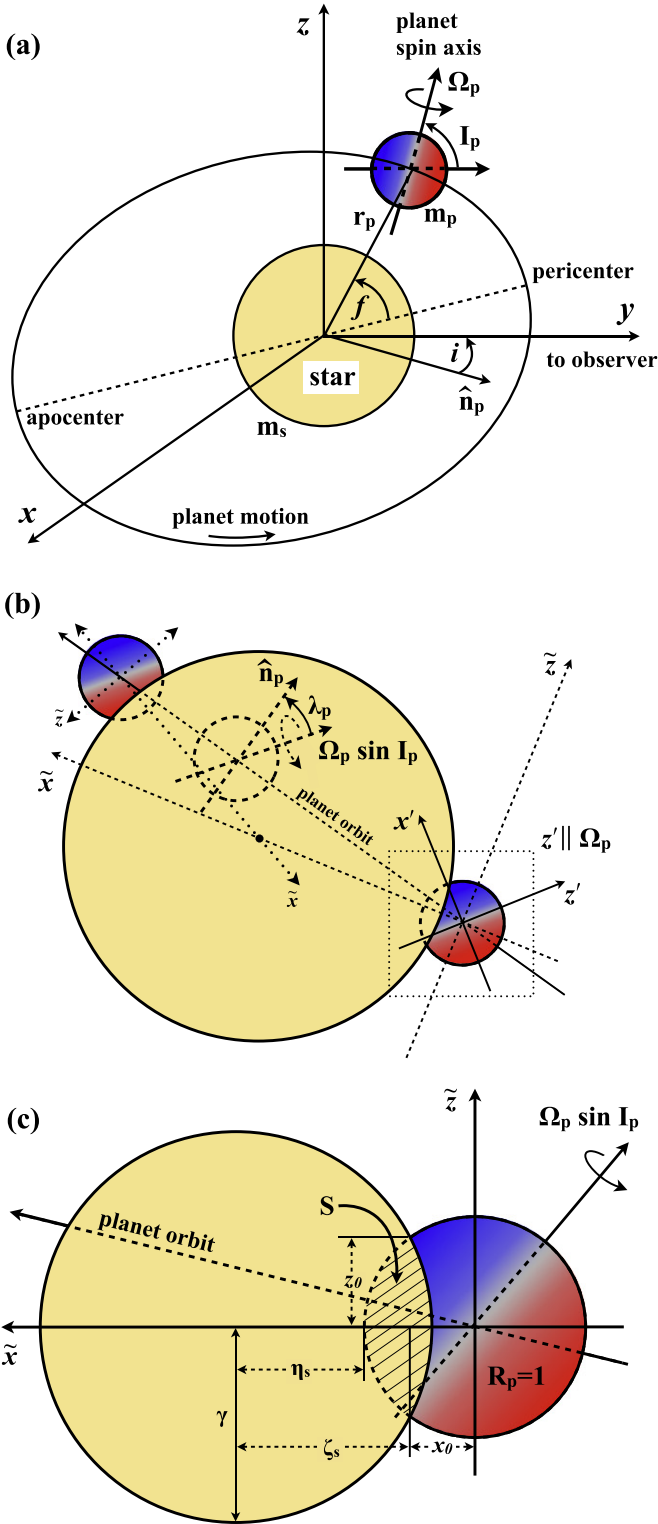$$v_p = \Omega_p x' \sin I_p, \quad (2)$$

Figure 1. (a) Schematic illustration of the planetary orbit plane, spin axis, and the observer's line of sight; (b) planet secondary eclipse ingress and egress phases and rotation axis; (c) a zoom of the planet and star configuration at ingress in the new coordinates (see Table 1 for symbol definitions).

where Ω_p is the angular velocity of the planet. The associated radiation will exhibit a Doppler shift defined as
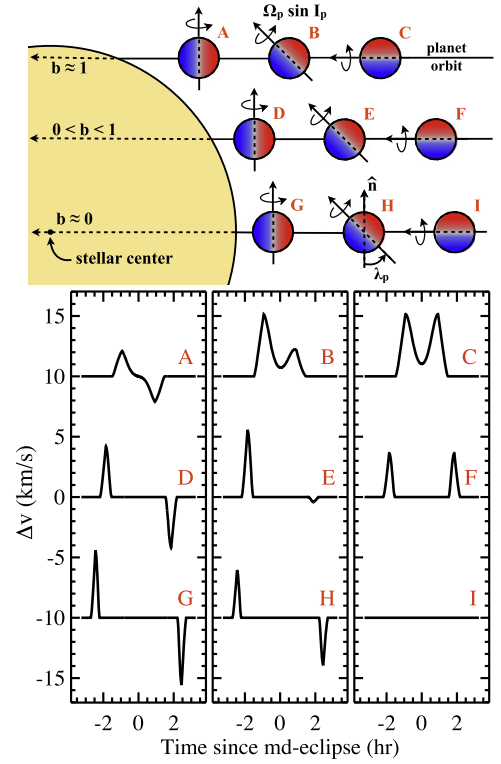
$$\frac{\Delta\nu}{\nu} = \frac{\Omega_p x' \sin I_p}{c}, \tag{3}$$

Figure 2. Illustration of planet radial velocity curve anomaly due to RMse effect for nine (representative) prograde spin–orbital alignments. The curves are plotted with a constant 10 km s^{-1} offset for clarity. Cases A–I correspond to the top planet–star configurations. The curves flip and invert as λ_p increases to 360° and when $b < 0$.

with respect to the observer along the y'-axis (i.e., the line of sight). We refer the reader to Section 3, Equations (14)–(19) in Ohta et al. (2005) for a derivation of the radial velocity profile for a star and adopt their expression (20) rewritten for the planet:

$$\Delta v_p = -\Omega_p \sin I_p \frac{\iint x' I(x', z') dx' dz'}{\iint I(x', z') dx' dz'}. \tag{4}$$

Equation (4) relates the radial velocity change Δv_p and the line intensity $I(x', z')$. Figure 2 illustrates the different cases of the RMse.

We evaluate the integrals assuming uniform model of the planet surface intensity $I(x', z')$. We ignore the role of planet limb-darkening as our goal is to estimate the first order rotational effect, and leave inclusion of the limb-darkening for future investigations. We also consider the star to be completely optically thick.

At ingress and egress the position of the stellar disc satisfies the relation $R_s - R_p < (x_s'^2 + z_s'^2)^{1/2} < R_s + R_p$. In order to simplify the computational task we rotate the coordinates in a time-dependent manner so that the stellar center is always located along the new $\tilde{x}$-axis, as in Ohta et al. (2005), see Figure 1(b):

$$\begin{pmatrix} \tilde{x} \\ \tilde{z} \end{pmatrix} = \frac{1}{R_p \sqrt{x_s'^2 + z_s'^2}} \begin{pmatrix} x_s' & z_s' \\ -z_s' & x_s' \end{pmatrix} \begin{pmatrix} x' \\ z' \end{pmatrix}. \tag{5}$$

The position of the star is given by

$$\begin{pmatrix} \tilde{x}_s \\ \tilde{z}_s \end{pmatrix} = \begin{pmatrix} 1 + \eta_s \\ 0 \end{pmatrix}, \tag{6}$$

where η is defined as

$$\eta_s = \sqrt{\frac{x_s'^2 + z_s'^2}{R_p^2}} - 1. \tag{7}$$

The intensity on the uniform planet surface at $(\tilde{x}, \tilde{z})$ is given by

$$I(\tilde{x}, \tilde{z}) = \begin{cases} I_0, & \tilde{x}^2 + \tilde{z}^2 \leqslant 1 \text{ and } (\tilde{x} - 1 - \eta_s)^2 + \tilde{z}^2 \geqslant \gamma^2, \\ 0 & \text{otherwise}, \end{cases} \tag{8}$$

where $\gamma = R_s/R_p$, $R_p = 1$. The moments of the intensity then are

$$\iint I(x', z') \, dx' \, dz' = R_p^2 \left[\pi I_0 - \iint_S I(\tilde{x}, \tilde{z}) \, d\tilde{x} \, d\tilde{z} \right], \tag{9}$$

and

$$\iint x' I(x', z') \, dx' \, dz' = -\frac{R_p^2}{1 + \eta_s} \iint_S (x_s' \tilde{x} - z_s' \tilde{z}) \times I(\tilde{x}, \tilde{z}) \, d\tilde{x} \, d\tilde{z}. \tag{10}$$

The range of the integrals is denoted with S and is defined as the star–planet overlapping region (shaded area) in Figure 1(c):

$$\iint_S d\tilde{x} \, d\tilde{z} = \int_{x_0}^1 d\tilde{x} \int_{-\sqrt{1-\tilde{x}^2}}^{\sqrt{1-\tilde{x}^2}} d\tilde{z} + \int_{\tilde{x}_s - \gamma}^{x_0} d\tilde{x} \int_{-\sqrt{\gamma^2 - (\tilde{x} - \tilde{x}_s)^2}}^{\sqrt{\gamma^2 - (\tilde{x} - \tilde{x}_s)^2}} d\tilde{z}. \tag{11}$$

The star and planet circles intersect at $(x_0, \pm z_0)$, where

$$x_0 = 1 - \frac{\gamma^2 - \eta_s^2}{2(1 + \eta_s)}, \tag{12}$$

$$z_0 = \sqrt{1 - x_0^2} = \frac{\sqrt{(\gamma^2 - \eta_s^2)[(\eta_s + 2)^2 - \gamma^2]}}{2(1 + \eta_s)}. \tag{13}$$

These calculations are equivalent to the calculations presented in Ohta et al. (2005) and to simplify the final result we introduce

$$\zeta = 1 + \eta_s - x_0 = \frac{2\eta_s + \gamma^2 + \eta_s^2}{2(1 + \eta_s)}. \tag{14}$$

Then Equations (9) and (10) are analytically integrated as

$$\iint_S I(\tilde{x}, \tilde{z}) d\tilde{x} \, d\tilde{z} = I_0 \left[\sin^{-1} z_0 - (1 + \eta_s) z_0 + \gamma^2 \cos^{-1} \zeta/\gamma \right], \tag{15}$$

and

$$\iint_S (\tilde{x} x_s' - \tilde{z} z_s') I(\tilde{x}, \tilde{z}) d\tilde{x} \, d\tilde{z} = I_0 x_s' (1 + \eta_s) \left[-z_0 \zeta + \gamma^2 \cos^{-1} \zeta/\gamma \right]. \tag{16}$$

Finally combining these two results we find the radial velocity anomaly of the planet (during ingress or egress) as a function of the star position (x_s'):

$$\Delta v_p = \Omega_p x_s' \sin I_p$$
$$\times \frac{-z_0 \zeta + \gamma^2 \cos^{-1}(\zeta/\gamma)}{\pi - \sin^{-1} z_0 + (1 + \eta_s) z_0 - \gamma^2 \cos^{-1}(\zeta/\gamma)}. \tag{17}$$

The final result is equivalent to the result of Ohta et al. (2005) which is expected given the identical overlapping area between the planet and star circles.

4. RMse EFFECT AMPLITUDE AND SHAPE

The shape and amplitude of the RMse effect are illustrated in Figure 2 for nine representative configurations of the planet spin–orbital alignments (i.e., impact parameter $b = \frac{a}{R_*} \cos i$ and λ_p), corresponding to prograde rotation. In case of retrograde rotation (i.e., $\lambda_p \geqslant 90°$) the radial velocity curves are inverted. The RMse computation in Figure 2 assumes a Jupiter-like planet, with $v \sin I_p$ at the equator of 12.6 km s^{-1}, on a 20 day orbit around a Sun-like star. We choose a period rather longer than the currently typical hot-Jupiter orbital periods because close-in exoplanets are expected to rapidly synchronize their rotation with the orbital period due to tides raised by the star on the planet. The time to spin-down the planet rotation is given by

$$\tau_{syn} \approx Q_p \left(\frac{R_p^3}{GM_p} \right) (\omega - \omega_s) \left(\frac{M_p}{M_*} \right)^2 \left(\frac{a_p}{R_p} \right)^6, \tag{18}$$

where Q_p, R_p, M_p, ω, ω_s, M_*, and a_p are the planet's tidal dissipation factor, radius, mass, rotational angular velocity, and synchronous (or orbital) angular velocity (Goldreich & Soter 1966; Guillot et al. 1996). Assuming $Q_p \sim 10^5$ (Correia & Laskar 2010) and orbital periods of 4 and 20 days, we find $\tau_{syn} \sim 10^6$ and 10^9 years, respectively implying that a $\sim$20 day orbit required to have spin-down times comparable to the ages of the currently observed transiting hot Jupiters.

Our choice for the value of $v \sin I_p$ is driven by the correlation of the equatorial rotational velocities of solar system planets and their masses, suggesting that more massive planets rotate faster (Hughes 2003). Currently a rotational rate has been constrained only for the massive and young planet β Pic b ($v \sin I_p \sim 25$ km s^{-1}), which is in line with the spin velocity–mass relation of the solar system (Snellen et al. 2014).

The maximum amplitude of the RMse effect is expected for central eclipses (i.e., $b = 0$) and $\lambda_p = 0$ or 180°. In the case considered in Figure 2, the amplitude is $\pm \sim 6$ km s^{-1}. Assuming the $v \sin I_p$ of β Pic b we find rotation effect with an amplitude of $\sim$11 km s^{-1}. No effect is expected in cases where equal portions red and blueshifted portions of the planet are eclipsed (i.e., $b = 0$ and $\lambda_p = 90°$ or 180°). This is also the case where the planet rotation axis is normal to the plane of the sky.

It should be pointed out that in all cases that include $b = 0$, $v \sin I_p$ is degenerate with λ_p, i.e., various combinations of these two parameters can produce the same radial velocity amplitude. Importantly, it is the amplitude difference of the ingress and egress RMse, their signs and the shape of the radial velocity curve that constrain the planet obliquity and break this degeneracy.

4

5. AN OBSERVATIONAL PERSPECTIVE FOR RMse

We produce mock data to illustrate the planetary RMse effect assuming an 8 and 40 m class telescopes, equipped with a near-infrared, high spectral resolution (i.e., $R \sim 100,000$) spectrometer. We assume that the planet orbit is constrained with enough precision to be subtracted prior to the search for the RMse effect. We calibrate our simulation adopting a precision of $\sim 5\,\mathrm{km\,s^{-1}}$ as achieved by Birkby et al. (2013) at $3.2\,\mu\mathrm{m}$ for water detection in the day side atmosphere of HD 189733b. We scale this precision by the square root of the number of collected spectra (i.e., 48), the ratio of the employed spectral coverage (assuming a hypothetical high-resolution spectrometer with a wavelength coverage of 400 nm) and a square root of the ratio of the target planet-to-star flux ratio and the planet-to-star flux ratio of HD 189733b, i.e., 1.3×10^{-3} from Birkby et al. (2013). This factor plays a critical role as it accounts for the strength of the planet signal, which is determined by the planet-to-star flux contrast. The contrast decreased from $\sim 10^{-3}$ to $\sim 10^{-6}$ when increasing the planet orbital periods from ~ 0.5 to 20 days. We also factor in the sampling rate with the telescope diameter and the brightness of the target host star. An account for the change of the planet flux during a secondary eclipse is also incorporated by factoring the radial velocity uncertainties by square root of the flux of a secondary eclipse Mandel & Agol (2002) model with unity out-of eclipse baseline and zero in-eclipse flux.

Figure 3 shows mock data generated assuming a 40 m-class telescope and a hypothetical planet host star of brightness $K = 5.5$ mag (i.e., similar to the currently brightest transiting hot-Jupiter host star HD 189733). Figure 3 shows the results for a planet with the physical properties of WASP-19 b, which is considered to be tidally locked. We assumed a prograde ($\lambda_\mathrm{p} = 35°$) and a retrograde ($\lambda_\mathrm{p} = 215°$) rotation with $v \sin I_\mathrm{p} = 8\,\mathrm{km\,s^{-1}}$. We perform a RMse fit to the mock data utilizing a Levenberg–Marquardt least-squares minimization and estimate λ_p and $v \sin(I_\mathrm{p})$, (Markwardt 2009). We find the planet signal to be well-detected ($\sim 5\,\sigma$) when combining nine secondary eclipses.

We also explored the potential of an 40 m-class telescope to detect the RMse effect in the currently brightest transiting exoplanet host-star HD 189733b. Assuming a synchronized planet rotation (i.e., RMse amplitude of $\sim 1\,\mathrm{km\,s^{-1}}$) and $\lambda_\mathrm{p} > 0°$ we find that ~ 50 secondary eclipses need to be co-added to detect the spin of HD 189733b.

Finally, we investigated the potential of an 8 m-class telescope to detect the RMse effect in $K = 5.5$ host star with a WASP-19b-like planet and synchronized rotation. We find a number of ~ 50 secondary eclipses will have to be added in order to detect the RMse effect at $\sim 3\,\sigma$ confidence.

6. DISCUSSION AND CONCLUSIONS

We have discussed the Doppler signature of a spinning exoplanet during secondary eclipse and derived a relation for the radial velocity as a function of the planet's rotational rate and axial tilt (Equation (17)). The RMse effect complements the tool-box offered by transiting exoplanets providing a proxy to exoplanet spins. We showed that the formalism of the RMse is equivalent to the formalism developed by Ohta et al. (2005) to describe the RM effect caused by a planet transiting its star just from a different perspective. We note that Hirano et al. (2011) derived an improved accuracy radial velocity anomaly
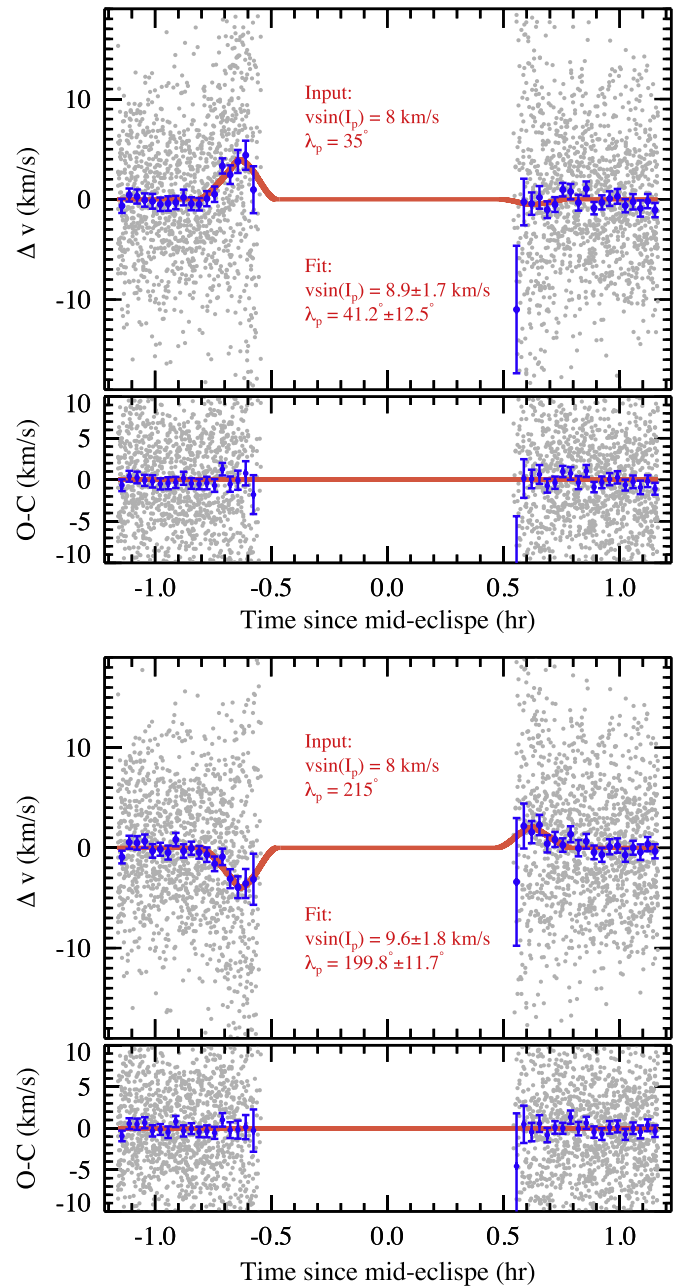

Figure 3. Mock data (gray dots) illustrating the RMse effect, best-fit radial velocity curve (red lines), and radial velocity residuals. Upper and lower pair panels illustrate the cases of a WASP-19 system, assuming tidally synchronized prograde and a retrograde rotating planet, respectively. The blue symbols indicate the binned radial velocity curves by 2 minutes.

curves for the RM effect during primary transits. However, the solution of Ohta et al. (2005) provides a conservative estimate of the radial velocity amplitude and is precise enough to illustrate the RMse effect.

We acknowledge that our assumption of a rigid rotating non-limb darkened planetary surface (i.e., ignoring differential rotation and atmospheric dynamics) is a crude approximation, but it illustrates the expected RMse radial velocity anomaly in the simplest case. The radial velocity originating from the RMse effect is expected to be degenerate with atmospheric dynamics. Exoplanets are expected to have atmospheric circulation with increasing dynamics at shorter orbital distances (Kataria et al. 2015). Therefore, it is expected that the radial

velocity curves of most close-in exoplanets may significantly differ from that assumed here, with super-rotating winds expected to enhance the radial velocity signals by factor of a few. The RMse effect presents the opportunity to probe atmospheric winds with altitude, when wide coverage high dispersion spectroscopy becomes capable of providing per-point precisions in the $\sim$m s^{-1} domain. In such cases it could be possible to measure longitudinally integrated radial velocities and map the surface of a planet during the secondary eclipse ingress/egress phases, providing constraints on the hot-spot position. We postpone the derivation of the RMse effect in these cases for future theoretical global circulation model investigations and identify the top three planets expected to exhibit the strongest RMse effect assuming synchronized rotation. Applying Equation (17) (assuming $\lambda_p = 0°$) we find values of $\Delta v_p \sim$ 3.7, 3.4, and 3 km s^{-1} for targets WASP-103 b, WASP-12 b and WASP-19 b, respectively.

Kawahara (2012) demonstrated the rotational signature of an exoplanet in the planet radial velocity. The RMse effect discussed in this study is of similar nature. However the geometric shadow of the star rather than the changing planet phase is the factor removing velocity components from the visible planet surface. Importantly, because the RMse effect occurs only during ingress and egress, its detection requires significantly less observing time compared to the case in Kawahara (2012). RMse therefore could be much-well suited for planets with longer orbital periods.

We also demonstrated that to be put into practice the RMse effect requires exoplanet host stars brighter than the currently known exoplanet hosts, i.e., brighter than $K \sim 6$ mag and large aperture telescopes (i e. $\sim$40 m). The strongest RMse effect for evolved stars is expected for non-synchronized rotation, i.e., planets on longer than 20 day orbits, with a typical $v \sin I_p$ 12.5 km s^{-1} or more. However, such planets exhibit lower temperatures (i.e., <700 K), compared to the typical hot Jupiters giving a small planet-to-star flux contrasts (i.e., $\sim 10^{-6}$ or lower at ~ 3 μm). The detection of the RMse effect in such cases would be an extremely challenging if not impossible task, even for the upcoming 40 m class telescopes.

An interesting case could be young planets which still have not been synchronized. Observations using high-dispersion, near-infrared spectroscopy have currently constrained the rotational rate of the only one such case (β Pic b) from rotationally broadened absorption lines (Snellen et al. 2014). An important opportunity could exist if the orbit orientation of this planet allows transits and secondary eclipses, because the large brightness of the host star (i.e., $K \sim 3.5$ mag) and the fast spin of the planet (i.e., $v \sin I_p \sim 27$ km s^{-1}) would produce a strong and detectable RMse signal. Another interesting opportunity could be offered by transiting brown dwarfs with orbital periods larger than 10–20 days. Such systems assume high flux contrasts between the star and the brown dwarf in the near-infrared which in case of a bright host star (i.e., $K \sim 5$ mag) could provide an opportunity to probe the spins and latitudinal radial velocity maps of these objects.

In the near future, the Next Generation of Transit Surveys, the *Transiting Survey Satellite*, and the Planetary Transits and Oscillations of stars projects are expected to significantly expand the sample of known planets hosted by bright stars (i.e., brighter than $K \sim 9.5$ mag) and hence to provide more targets suitable for detection of the RMse effect.

The hypothetical radial velocity data in Section 5 assumes retrieval of the planet signal via cross-correlation with a model planet spectrum similar to Snellen et al. (2010), Brogi et al. (2012), Birkby et al. (2013), de Kok et al. (2013), and Schwarz et al. (2015). Although currently the cross-correlation technique has not been demonstrated to provide per spectrum radial velocity measurements, in their Figure 1, Snellen et al. (2010) presented results for the planet geocentric radial velocity as a function of the planet orbital phase at a high significance ($\sim 3 \sigma$). It is expected that large-aperture near-future telescopes (i.e., 30–40 m) could provide even higher significance signals and planet radial velocity measurements from multiple spectra. In addition, cloud-free exoplanet atmospheres are expected to result in stronger cross-correlation signals compared to hazy or cloudy atmospheres for the same stellar and planetary physical properties. Cloud-free atmospheres are expected to have well-pronounced lines, i.e., non-muted absorption features which are not expected for hazy atmospheres.

Stellar activity and pulsations are known to produce radial velocity variations that could in some cases mimic those induced by the orbital motion of exoplanets. This may lead to misinterpretations of radial velocity variations, especially when those variations have periods less or equal to the star rotational periods (Lagrange et al. 2010). Therefore, it is important to consider whether stellar activity, for instance the distortion to the stellar spectral lines induced by starspots on a rotating stellar surface, could induce residual signal misinterpreted as exoplanet signal. This is especially pertinent for co-added observations obtained over several nights.

A typical RMse observation would last for $\sim$0.8 hr on each of the ingress and egress phases of a WASP-19b-like planet (see Figure 3). This time interval is significantly shorter than the rotation periods of the typical planet host stars ranging from 10 to 40 days (Paz-Chinchón et al. 2015). Furthermore, starspots are expected to produce sine-wave radial velocity variations (i.e., different from the RMse shape) with amplitudes of a few hundred m s^{-1} in the optical and are expected to reduce by factor of at least a few at near-infrared wavelengths, where the contrast between the photosphere and cool star spots (e.g., $\Delta T \sim 550$ K) is significantly reduced.

Thus, if present, residual stellar signal caused by starspots would be a factor of a few tens smaller than the the expected 1–2 km s^{-1} amplitude of the RMse effect for the closest synchronized planets and even more for non-synchronized planets on longer than 20 day period orbits. Only in the case of most evolved planets (i.e., typical hot Jupiters), if synchronized, with orbital/rotational periods from 4–5 to <20 days could a residual introduce larger radial velocity scatter when multiple observations are combined. However, such planets are expected to have RMse amplitudes much smaller than 1 km s^{-1} and would be difficult targets by definition.

In the near-infrared the planet spectrum is dominated by thermal radiation and is not expected to contain information from distortions caused by starspots. In case that the planet spectrum also contains a non-negligible component from a reflected star spectrum then the planet spectral lines will have distortions caused by the star spots. This would make the planet spectrum different and more difficult to cross correlate with model spectra. However, such an effect is not expected to mimic the RMse.

In conclusion, we have demonstrated the RMse effect and its potential to constrain planet rotational rates and sky projected spin–orbital alignments. We derived the radial velocity curve caused by the RM anomaly and estimated the amplitude of the

effect for a hot Jupiter. Finally we discussed the prospects for detecting the effect and constraining planet spins and axial tilts from the current and upcoming instrumentation.

REFERENCES

Agnor, C. B., Canup, R. M., & Levison, H. F. 1999, Icar, 142, 219
Barnes, J. W., & Fortney, J. J. 2003, ApJ, 588, 545
Birkby, J. L., de Kok, R. J., Brogi, M., et al. 2013, MNRAS, 436, L35
Brogi, M., de Kok, R. J., Birkby, J. L., Schwarz, H., & Snellen, I. A. G. 2014, A&A, 565, A124
Brogi, M., Snellen, I. A. G., de Kok, R. J., et al. 2012, Natur, 486, 502
Correia, A. C. M., & Laskar, J. 2010, in Exoplanets, ed. S. Seager (Tuscon, AZ: Univ. Arizona Press), 22, 239
Cowan, N. B., Voigt, A., & Abbot, D. S. 2012, ApJ, 757, 80
Cox, A. N., & Pilachowski, C. A. 2000, PhT, 53, 77
de Kok, R. J., Brogi, M., Snellen, I. A. G., et al. 2013, A&A, 554, A82
de Pater, I., & Lissauer, J. J. 2001, in Planetary Sciences, ed. I. de Pater & J. J. Lissauer (Cambridge: Cambridge Univ. Press), 544
Faure, G., & Mensing, T. M. (ed.) 2007, in Introduction to Planetary Science: The Geological Perspective (Berlin: Springer)
Fujii, Y., & Kawahara, H. 2012, ApJ, 755, 101
Goldreich, P., & Soter, S. 1966, Icar, 5, 375
Guillot, T., Burrows, A., Hubbard, W. B., Lunine, J. I., & Saumon, D. 1996, ApJL, 459, L35
Heller, R., Barnes, R., & Leconte, J. 2011, OLEB, 41, 539
Heller, R., Leconte, J., & Barnes, R. 2011, A&A, 528, A27
Hirano, T., Suto, Y., Winn, J. N., et al. 2011, ApJ, 742, 69
Hughes, D. W. 2003, P&SS, 51, 517
Hui, L., & Seager, S. 2002, ApJ, 572, 540
Kataria, T., Showman, A. P., Fortney, J. J., et al. 2015, ApJ, 801, 86
Kawahara, H. 2012, ApJL, 760, L13
Kawahara, H., & Fujii, Y. 2010, ApJ, 720, 1333
Lagrange, A.-M., Desort, M., & Meunier, N. 2010, A&A, 512, A38
Laskar, J., & Robutel, P. 1993, Natur, 361, 608
Mandel, K., & Agol, E. 2002, ApJL, 580, L171
Markwardt, C. B. 2009, adass XVIII, 411, 251
McLaughlin, D. B. 1924, ApJ, 60, 22
Murray, C. D, & Dermott, S. F. 1999, in Solar System Dynamics, ed. C. D. Murray (Cambridge: Cambridge Univ. Press), 1999
Ohta, Y., Taruya, A., & Suto, Y. 2005, ApJ, 622, 1118
Pallé, E., Ford, E. B., Seager, S., Montañés-Rodríguez, P., & Vazquez, M. 2008, ApJ, 676, 1319
Paz-Chinchón, F., Leão, I. C., Bravo, J. P., et al. 2015, ApJ, 803, 69
Rossiter, R. A. 1924, ApJ, 60, 15
Schwarz, H., Brogi, M., de Kok, R., Birkby, J., & Snellen, I. 2015, A&A, 576, A111
Seager, S., & Hui, L. 2002, ApJ, 574, 1004
Snellen, I. A. G., Brandl, B. R., de Kok, R. J., et al. 2014, Natur, 509, 63
Snellen, I. A. G., de Kok, R. J., de Mooij, E. J. W., & Albrecht, S. 2010, Natur, 465, 1049
Williams, D. M., & Kasting, J. F. 1997, Icar, 129, 254
Winn, J. N., Noyes, R. W., Holman, M. J., et al. 2005, ApJ, 631, 1215